Theoretical Study of the Electronic Nonadiabatic Transitions in the Photoelectron Spectroscopy of F_2O

Gireesh M. Krishnan,† Subhas Ghosal, and Susanta Mahapatra*

School of Chemistry, University of Hyderabad, Hyderabad 500 046, India

Received: August 6, 2005; In Final Form: November 12, 2005

The photoelectron spectrum of F_2O pertaining to ionizations to the ground ($\tilde{X}^2B_1$) and low-lying excited electronic states ($\tilde{A}^2B_2$, $\tilde{B}^2A_1$, and $\tilde{C}^2A_2$) of F_2O^+ is investigated theoretically. The near equilibrium potential energy surfaces of the ground electronic state ($\tilde{X}^2B_1$) of F_2O and the mentioned ground and excited electronic states of F_2O^+ reported by Wang et al. (*J. Chem. Phys.* **2001**, *114,* 10682) for the C_{2v} configuration are extended for the C_s geometry assuming a harmonic vibration along the asymmetric stretching mode. The vibronic interactions between the $\tilde{A}^2B_2$ and $\tilde{B}^2A_1$ electronic states of F_2O^+ are treated within a linear coupling approach, and the strength of the vibronic coupling parameter is calculated by an ab initio method. The nuclear dynamics is simulated by both time-independent quantum mechanical and time-dependent wave packet approaches. Although the first photoelectron band exhibits resolved vibrational progression along the symmetric stretching mode, the second one is highly overlapping. The latter is attributed to the nonadiabatic interactions among the energetically close $\tilde{A}^2B_2$, $\tilde{B}^2A_1$, and $\tilde{C}^2A_2$ electronic states of F_2O^+. The theoretical findings are in good accord with the available experimental results.

I. Introduction

Spectroscopy and dissociation dynamics of halogen oxides have attracted increasing attention in the literature because of their relevance in the photochemistry of the stratosphere and apparently they are involved, directly or indirectly, in the depletion of ozone layer.[1] The molecules of oxygen and chlorine have been studied extensively both experimentally and theoretically.[2−8] In contrast, the photophysics and photochemistry of difluorine oxide, F_2O, has received only scant attention in the literature.[10−12] The photoelectron spectra of halogen dioxide and dihalogen oxides are found to be particularly appealing because they bear signatures of strong nonadiabatic interactions in the excited electronic states.[6−9] The photoelectron spectra usually have poor energy resolution; however, they are often used to estimate the extent of nonadiabatic interactions among the participating electronic states and thereby facilitate the development of theoretical models to examine the nuclear dynamics in the excited electronic states.

F_2O is a nonlinear triatomic molecule with a C_{2v} symmetry at its equilibrium configuration. The ultraviolet photoelectron spectrum of F_2O was first recorded by Conford and co-workers[10] and then by Brundle and co-workers.[11] The observed bands were assigned based on the semiempirical electronic structure data. Both of these experiments assigned the first four electronic states of F_2O^+ in the order $^2B_1$, $^2A_1$, $^2B_2$, and $^2A_2$. An alternative assignment was also proposed by Brundle and co-workers[11] in which the overlapping second, third, and fourth photoelectron bands were assigned to the $^2A_1$, $^2B_2$, and $^2A_2$ electronic states. Theoretical calculations of the ionization energies of the low-lying electronic states of F_2O^+ appeared thereafter.[13] However, the energetic ordering of the three cationic states ($^2A_1$, $^2B_2$, and $^2A_2$) still remained controversial. Recently, Wang et al.[12] reported high-level ab initio calculation on the near equilibrium C_{2v} potential energy surfaces (PESs) of the ground electronic state of F_2O and the ground and the low-lying excited states of F_2O^+. The three excited electronic states of the latter are shown to be $^2B_2$, $^2A_1$, and $^2A_2$ in order of ascending energy. This energetic ordering was reconfirmed latter by Tomasello et al.[14] by symmetry-adapted cluster-configuration-interaction calculations. Wang et al.[12] also reported the harmonic and anharmonic Franck−Condon (FC) simulation of the photoelectron bands employing the C_{2v} PESs developed by them and have shown that the results are generally in good agreement with the experiment. None of the theoretical studies to date have considered any nonadiabatic interactions in the excited electronic states and their impact on the photoelectron spectrum of F_2O.

In this paper we revisit the photoelectron bands of F_2O and study them theoretically with the aid of a time-dependent wave packet (WP) as well as a Lanczos based time-independent quantum mechanical approach.[15−18] We consider the relevant nonadiabatic interactions in the excited electronic states of F_2O^+ and modeled them in our theoretical approach. The PESs reported by Wang et al.[12] for the C_{2v} geometry of F_2O and F_2O^+ are extended to the C_s configurations in this study, assuming a harmonic vibration along the asymmetric stretching mode. The electronic nonadiabatic interactions between the $\tilde{A}^2B_2$ and $\tilde{B}^2A_1$ excited electronic states of F_2O^+ are modeled by devising a diabatic electronic Hamiltonian within a linear vibronic coupling approach.[15] The linear vibronic coupling parameter is calculated by an ab initio method, and a conical intersection[15,19] between the two electronic states is established. The spin−orbit (SO) interactions between the near-degenerate $\tilde{B}^2A_1$ and $\tilde{C}^2A_2$ electronic states of F_2O^+ are not considered in this study primarily because of relatively small SO coupling due to the F atom. We have considered ∼10% contribution of the $\tilde{C}^2A_2$ band to the composite overlapping second and third photoelectron bands. The importance of the nonadiabatic interactions between

* Corresponding author. E-mail: smsc@uohyd.ernet.in. Fax: +91-40-23012460.

† Present address: Institut für Chemie und Biochemie, Physikalische und Theoretische Chemie, Freie Universität Berlin, Berlin, D-14195, Germany.

10.1021/jp0543882 CCC: $33.50
Published on Web 12/15/2005

the $\tilde{A}^2B_2$ and $\tilde{B}^2A_1$ electronic states is further examined by monitoring the nonradiative decay of the electronic population in the coupled electronic manifold. It is worthwhile to carry out the femtosecond time-resolved experiment to verify the above predictions and the validity of the present vibronic coupling model.

We also calculated the first photoelectron band of F_2O and find that it compares well with the experimental results at low energy resolution. The peaks in the spectrum are ~0.13 eV spaced in energy, which corresponds to a progression along the symmetric stretching mode of F_2O^+. The major contribution to the intensity of the overlapping second photoelectron band comes from the interacting $\tilde{A}^2B_2$ and $\tilde{B}^2A_1$ electronic states, and a minor contribution is considered from the $\tilde{C}^2A_2$ electronic state. The theoretical results compare well with the experimental recording.[12]

The rest of the paper is organized in the following way. In section II we discuss the ab initio calculations of the vibronic coupling parameter and describe the theoretical framework to treat the nuclear dynamics by the time-dependent wave packet and the time-independent quantum mechanical approaches. The results are presented and discussed in section III, and the summarizing remarks are presented in section IV.

II. Theoretical Framework

A. Vibronic Hamiltonian. The first photoelectron band of F_2O pertinent to a transition to the $\tilde{X}^2B_1$ electronic state of F_2O^+ is essentially described by the nuclear motion on the Born−Oppenheimer PES of the latter. This is because the ground electronic state of F_2O^+ is energetically well separated (~4.56 eV at the equilibrium configuration) from its first excited electronic state. The second, third, and fourth photoelectron bands, however, are highly overlapping and are proposed here to be due to the nonadiabatic interactions among the three low-lying near-degenerate excited electronic states ($\tilde{A}^2B_2$, $\tilde{B}^2A_1$, and $\tilde{C}^2A_2$) of F_2O^+. To describe the associated nonadiabatic interactions, we resort to a diabatic electronic representation[20] in which the coupling between the states is described by smoothly varying off-diagonal elements of the electronic Hamiltonian. This is to be contrasted with the corresponding adiabatic electronic representation in which the coupling between the states is described by the off-diagonal elements of the nuclear Hamiltonian and these elements exhibit a singularity at the seam of intersections of the electronic states. In absence of any relativistic effects, the representative Hamiltonian to describe the first four photoelectron bands of F_2O is given by

$$\mathscr{H} = \mathscr{H}^{\mathrm{Nu}} + \mathscr{H}^{\mathrm{el}} = T_N \begin{pmatrix} 1 & 0 & 0 & 0 \\ 0 & 1 & 0 & 0 \\ 0 & 0 & 1 & 0 \\ 0 & 0 & 0 & 1 \end{pmatrix} + \begin{pmatrix} \mathscr{U}_{11} & 0 & 0 & 0 \\ 0 & \mathscr{U}_{22} & \mathscr{U}_{23} & 0 \\ 0 & \mathscr{U}_{32} & \mathscr{U}_{33} & 0 \\ 0 & 0 & 0 & \mathscr{U}_{44} \end{pmatrix} \quad (1)$$

where $\mathscr{H}^{\mathrm{Nu}}$ and $\mathscr{H}^{\mathrm{el}}$ represent the nuclear and the electronic part of the Hamiltonian matrix, respectively, T_N is the nuclear kinetic energy operator, and $\mathscr{U}_{ii}$ describes the potential energies of the electronic states of F_2O^+ ($i = 1$, 2, 3, and 4 refer to the $\tilde{X}^2B_1$, $\tilde{A}^2B_2$, $\tilde{B}^2A_1$, and $\tilde{C}^2A_2$ electronic states, respectively). The quantity $\mathscr{U}_{23} = \mathscr{U}_{32}$ represents the nonadiabatic coupling potential between the $\tilde{A}^2B_2$ and $\tilde{B}^2A_1$ electronic states.

F_2O is a bent molecule and has a C_{2v} minimum in the neutral ground electronic state and the cationic ground and excited electronic states. To exploit this symmetry explicitly in the nuclear dynamical simulations, we express the elements of the above Hamiltonian matrix in terms of the symmetry-adapted Jacobi coordinates pertinent to the C_{2v} point group in the body-fixed frame. In the following, we refer to r_v as the distance between the two terminal F atoms, r_d as the distance between the O atom to the center-of-mass of the two F atoms, and γ as the angle between $\vec{r}_v$ and $\vec{r}_d$. Use of such symmetry-adapted Jacobi coordinates for the present example is advantageous over hyperspherical coordinates[21] because it leads to a block-diagonal structure of the Hamiltonian based on the vibronic symmetries. This fact simplifies the numerical computation significantly by reducing the grid size by a factor of 2, when the $\tilde{A}^2B_2-\tilde{B}^2A_1$ coupled electronic manifold is considered. A hyperspherical coordinate system, however, is most suitable for a similar triatomic system belonging to the D_{3h} symmetry point group. In terms of the symmetry-adapted Jacobi coordinates, the nuclear kinetic energy operator for the total angular momentum $J = 0$ is given by

$$T_N = -\frac{\hbar^2}{2\mu}\frac{\partial^2}{\partial r_d^2} - \frac{\hbar^2}{2\mu'}\frac{\partial^2}{\partial r_v^2} - \frac{\hbar^2}{2I}\frac{1}{\sin\gamma}\frac{\partial}{\partial\gamma}\left(\sin\gamma\frac{\partial}{\partial\gamma}\right)$$

$$\mu = \frac{m_F m_0}{m_F + 2m_O}$$

$$\mu' = \frac{m_F}{2}$$

$$\frac{1}{I} = \frac{1}{\mu r_d^2} + \frac{1}{\mu' r_v^2} \quad (2)$$

The quantities m_F, m_O, and I denote the masses of the fluorine and oxygen atoms and the three-body moment of inertia, respectively.

B. Details of the Electronic Potential Energy Surfaces and the Vibronic Coupling Parameter. The elements of the electronic Hamiltonian matrix, $\mathscr{H}^{\mathrm{el}}$, of eq 1 have been determined in the following way. For the dependence of potential energy surfaces $\mathscr{U}_{11}$, $\mathscr{U}_{22}$, $\mathscr{U}_{33}$, and $\mathscr{U}_{44}$ on the symmetric stretch coordinate, $S_1 = (\Delta r_1 + \Delta r_2)/\sqrt{2}$ (Δr_1 and Δr_2 are the displacements in FO bond lengths) and bending coordinates, $S_2 = \Delta\theta + \alpha\Delta\theta^2 + \beta\Delta\theta^3$, ($\Delta\theta$ being the displacements in FOF bond angle; α and β are related by an expression, $\beta = [1 + 3\alpha(\pi - \theta_{\mathrm{eqm}})^2]/[-2(\pi - \theta_{\mathrm{eqm}}]$, by restricting the energy gradient in S_2 to zero when the molecule is linear, θ_{eqm} is the equilibrium value of the FOF angle), that is, for C_{2v} geometries, the MRCI potential energy functions derived from the large-scale CASSCF/RCCSD(T)/cc-pVQZ calculations by Wang et al.[12] is used. These authors have fitted the potential energies to a polynomial of the form

$$V = \sum_{ij} C_{ij}(\Delta S_1)^i(\Delta S_2)^j + V_{\mathrm{eqm}} \quad (3)$$

The above function for the ground electronic state of F_2O and F_2O^+ is described by 16 coefficients and by 14 coefficients for the excited electronic states of F_2O^+. The quantity V_{eqm} is the potential energy at the equilibrium configuration in the respective electronic state. The details of the calculations can be found in ref 12. The dependence of these PESs on the asymmetric stretch coordinate, $S_3 = (\Delta r_1 - \Delta r_2)/\sqrt{2}$, is approximated by a Harmonic potential, $V(S_3) = \kappa_u S_3^2/2 = \omega_u Q_u^2/2$. The quantity κ_u is the force constant along the asymmetric stretching vibration (u symmetry), and ω_u is the harmonic vibrational frequency. The quantity Q_u represents the dimensionless normal coordinate of the asymmetric stretching vibration (see the details below).

The harmonic approximation along the asymmetric stretching motion is employed because the mentioned photoelectron bands of F_2O apparently do not show any noticeable excitation along this vibration.

We devote some space here to introduce the dimensionless normal coordinates. These are denoted as Q_{g1}, Q_{g2}, and Q_u for the symmetric stretching, bending, and asymmetric stretching vibrational motions of F_2O in its ground electronic state pertinent to the C_{2v} symmetry point group. The vibrational motion in this state is treated as harmonic. The mass-weighted normal coordinates of F_2O are then calculated by the *GF*-matrix method of Wilson et al.[22] using the experimentally derived force field of Pierce et al.[23] They are then transformed to the dimensionless normal coordinates by multiplying by $(\omega_i/\hbar)^{1/2}$ (ω_i is the frequency of the ith vibrational mode). The frequencies of the asymmetric stretching vibration of the neutral and cationic electronic states used to describe the PESs employed in this study are 0.1137, 0.1670, 0.1678, 0.2246, and 0.0714 eV for the ground electronic states of F_2O and the $\mathscr{U}_{11}$, $\mathscr{U}_{22}$, $\mathscr{U}_{33}$, and $\mathscr{U}_{44}$ electronic states of F_2O^+ reported by Wang et al.[12] The diabatic coupling potential between $\mathscr{U}_{22}$ and $\mathscr{U}_{33}$ is assumed to be a linearly varying function of Q_u, $\mathscr{U}_{23} = \mathscr{U}_{32} = \lambda Q_u$, λ being the linear vibronic coupling parameter. We note that the present model treats all of the higher order couplings in the Hamiltonian along the symmetric stretch and bending coordinates, whereas a linear coupling scheme is applied to the asymmetric stretch coordinate only.

The interstate linear vibronic coupling parameter, λ, is derived from the difference of the adiabatic potential energies of the $\tilde{A}^2B_2$ and $\tilde{B}^2A_1$ electronic states, calculated for the various C_s geometries of F_2O^+. The two are related via[15]

$$\lambda = \frac{1}{2} Q_u^{-1} \{[V_2(Q_u) - V_1(Q_u)]^2 - [V_2(\mathbf{Q_0}) - V_1(\mathbf{Q_0})]^2\}^{1/2} \tag{4}$$

where V_1 and V_2 are the adiabatic potential energies of the $\tilde{A}^2B_2$ and $\tilde{B}^2A_1$ electronic states, respectively, for the distorted nuclear configuration, Q_u. The latter is chosen in the vicinity of $\mathbf{Q_0}$ (equilibrium configuration of the ground electronic state of F_2O), $Q_u = \mathbf{Q_0} \pm \delta$, with δ being the small shift applied to change the symmetry point group from C_{2v} at $\mathbf{Q_0}$ to C_s at Q_u.

To calculate λ, we perform ab initio calculations for adiabatic potentials V_2 and V_1 for different values of Q_u around the equilibrium geometries of the neutral and cationic electronic states. We have also optimized the equilibrium geometry of the ground electronic state of F_2O employing the correlation consistent polarized valence triple-ζ (cc-pVTZ) Gaussian basis sets of Dunning.[24] The electronic structure calculations are performed using the GAUSSIAN[25] program package. The effect of electron correlation is treated by the second-order Møller−Plesset perturbation theory (MP2). This yields r (O−F bond length) = 1.40 Å and θ (F−O−F angle) = 103.17° for the optimized ground-state equilibrium geometry of F_2O to be compared to the corresponding values derived from microwave spectroscopy, $r = 1.4053$ Å and $\theta = 103.07°$.[12] We performed direct calculations of the vertical ionization energies of F_2O using the outer-valence Green's function (OVGF) method employing the same cc-pVTZ basis set and equated them to the adiabatic potential energies V_1 and V_2. The Green's function calculations are carried out for the following combinations of r and ϕ and for the displacement $\Delta r = 0.0$, 0.01, 0.1, and 0.2 Å: (i) $r = 1.4001$ Å, $\phi = 103.17°$ (MP2/cc-pVTZ equilibrium geometry of F_2O ground state); (ii) $r = 1.4053$ Å, $\phi = 103.07°$ (experimental equilibrium geometry of F_2O ground state); (iii) $r = 1.2715$ Å, $\phi = 107.99°$ (MP2/cc-pVTZ equilibrium geometry of the $\tilde{X}^2B_1$ state of F_2O^+); (iv) $r = 1.331$ Å, $\phi = 107.3°$ (IFCA (harmonic) equilibrium geometry of the $\tilde{X}^2B_1$ state of F_2O^+); (v) $r = 1.323$ Å, $\phi = 107.30°$ (IFCA (anharmonic) equilibrium geometry of the $\tilde{X}^2B_1$ state of F_2O^+); (vi) $r = 1.4437$ Å, $\phi = 82.28°$ (CCSD(T)/aug-cc-pVTZ equilibrium geometry of the $\tilde{A}^2B_2$ state of F_2O^+); and (vii) $r = 1.3689$ Å, $\phi = 118.57°$ (CCSD(T)/aug-cc-pVTZ equilibrium geometry of the $\tilde{B}^2A_1$ state of F_2O^+). The displacements are then transformed into dimensionless normal coordinates, and λ is calculated using the calculated OVGF data and eq 4. Such an analysis yields 0.05 eV $\leq \lambda \leq$ 0.28 eV, with an average value of $\lambda \approx 0.18$ eV.

III. Calculation of the Photoelectron Spectrum and Electronic Populations

The photoionization process is described by Fermi's Golden rule. The excitation function is given by

$$P(E) = \sum_{\mathrm{v}} |\langle \Psi_{\mathrm{v}} | \hat{T} | \Psi_0 \rangle|^2 \, \delta(E - E_{\mathrm{v}} + E_0) \tag{5}$$

where $|\Psi_0\rangle$ is the initial state; the vibrational and electronic ground state of the neutral F_2O with energy E_0, which is assumed to be vibronically decoupled from all other states. $|\Psi_{\mathrm{v}}\rangle$ is the final vibronic state of the radical cation with energy E_{v}. The operator $\hat{T}$ is the transition operator, which describes the interaction of the electron with the external radiation with energy E. In the present application, the initial and final states can be expressed as

$$|\Psi_0\rangle = |\phi^0\rangle|\chi_0^0\rangle \qquad |\Psi_{\mathrm{v}}\rangle = \sum_n |\phi^n\rangle|\chi_{\mathrm{v}}^n\rangle \tag{6}$$

where $|\phi\rangle$ and $|\chi\rangle$ refer to the (diabatic) electronic and vibrational parts of the wave function, respectively. The superscripts 0 and n refer to the electronic ground state of F_2O and excited nth electronic state of F_2O^+, respectively. Using eq 6, the spectral intensity can be rewritten within the Condon approximation as[15]

$$P(E) = \sum_{\mathrm{v}} |\tau^n \langle \chi_{\mathrm{v}}^n | \chi_0^0 \rangle| \, \delta(E - E_{\mathrm{v}} + E_0) \tag{7}$$

with

$$\tau^n = \langle \phi^n | \hat{T} | \phi^0 \rangle \tag{8}$$

being the transition operator matrix elements of the final electronic state n. In rewriting eq 7, the matrix elements of the transition operator are considered to be weakly varying functions of the nuclear coordinates. These elements are not calculated in the present study and are treated as constants (or adjusted empirically by examining the experimental data), in accordance with the applicability of the generalized Condon approximation in the diabatic electronic basis.[26]

To calculate the photoelectron spectrum using a time-dependent formalism, we used the Fourier transform representation of the Dirac delta function in the Golden rule formula in eq 7. The resulting expression can then be reduced to the Fourier transformation of the time autocorrelation function of the WP.[15,27] When the interacting electronic states possess different spatial symmetries, a vibronic symmetry exists and the vibronic secular matrix becomes block diagonal upon a suitable ordering

of basis states. The Golden rule expression is then rearranged to

$$P(E) \approx \sum_{k=1}^{n} |\tau^k|^2 \mathrm{Re} \int_0^\infty \mathrm{e}^{i(E+E_0)t/\hbar} C^k(t)\, \mathrm{d}t \qquad (9)$$

where the index k goes over to the component (diabatic) electronic states, $C^k(t) = \langle \chi^k(t=0)|\mathrm{e}^{-i\mathscr{H}t/\hbar}|\chi^k(t=0)\rangle$. The integral in eq 9 equals to i ($=\sqrt{-1}$) times the expectation value of the casual Green's function in the initial WP representation (see, for example, ref 15). Therefore, the imaginary part of this expectation value finally contributes to $P(E)$. The autocorrelation function is evaluated by solving the time-dependent Schrödinger equation numerically on a grid. For an explicitly time-independent Hamiltonian, the solution reads

$$\chi^k(t) = \exp[-i\mathscr{H}t/\hbar]\chi^k\,(t=0) \qquad (10)$$

We solve eq 10 numerically on a grid in the r_d, r_v, and γ space in order to calculate the wave function at time t from that at time $t = 0$. A 128×64 spatial grid is used in the $r_d \times r_v$ plane with $1.0\ a_0 \le r_d \le 4.556\ a_0$ and $1.0\ a_0 \le r_v \le 6.985\ a_0$. The grid along the Jacobi angle, γ, is chosen as the nodes of a 48-point Gauss-Legendre quadrature (GLQ). The action of the exponential operator on $|\chi^k\ (t=0)\rangle$ is carried out by dividing the total propagation time, t, into N steps of length Δt. The exponential operator at each Δt is then approximated by a second-order split-operator method,[28] adapted to the present coupled-state problem as discussed in the literature.[29] This is used in conjunction with the fast Fourier transform method to evaluate the exponential containing the radial kinetic energy operator[30] and with the discrete variable representation method to evaluate the exponential containing the rotational kinetic energy operator ($\boldsymbol{j}^2/2I$) on the wave function.[31] The latter is accomplished by transforming the grid wave function to the angular momentum basis (finite basis representation), multiplying it by the diagonal value of the operator ($\mathrm{e}^{-ij(j+1)\Delta t\hbar/4I}$), and then transforming it back to the grid representation. The WP is evolved for a total of 1.103 ps with a time step $\Delta t = 0.1347$ fs. The last 16 points of the grid along r_d and 8 points along r_v were covered with a damping function[32] in order to avoid any unphysical reflection or wraparound of the high-energy components of the WP that reach the finite-sized grid boundaries at longer time.

The initial vibrational wave function $|\chi_0^0\rangle$ pertinent to the ground electronic state of F_2O is calculated by a Lanczos-based relaxation method.[33] The ab initio potential energy surface for the ground electronic state of F_2O reported by Wang et al.[12] for the C_{2v} configurations is extended to the C_s geometries, assuming a harmonic vibration along the asymmetric stretching mode, and is used for the relaxation calculations. The time propagation is carried out by the short iterative Lanczos method[34] with variable time steps. This yields a zero point energy of 0.097 eV for the neutral F_2O. The ground vibrational wave function of the neutral obtained by this method is referred to as anharmonic in the rest of this paper. This initial wave function is then subjected to a FC transition and propagated with the final-state Hamiltonian (as discussed above). At each time step, the autocorrelation function is recorded and the spectral intensity is finally calculated using eq 9.

The time-dependence of the diabatic as well as adiabatic electronic populations are of immense importance in understanding the nonradiative decay dynamics of the optically prepared state mediated by the conical intersections.[15,35] These are calculated by defining adiabatic projectors in the diabatic electronic representation.[15,36]

In the following, we also report the results obtained by diagonalizing the vibronic Hamiltonian using the Lanczos algorithm[17] within a time-independent quantum mechanical framework. A similar grid as stated above is used for this purpose. In this method, the initial wave function is written as a direct product harmonic oscillator function along the Q_{g1}, Q_{g2}, and Q_u vibrational modes of F_2O. In this case, the intensity of the vibronic lines is shown to be the square of the first component of the Lanczos eigenvectors.[37] In case of the anharmonic initial wave function (discussed above), this formalism cannot be used and a filter diagonalization approach will be most effective.[38] This is beyond the scope of the present article and will be considered in a future study.

IV. Results and Discussion

In this section we show the photoelectron bands of F_2O calculated with the Hamiltonian of eq 1 and compare the theoretical results to the available experimental data.[10−12] The structure of the Hamiltonian matrix in eq 1 reveals that the nuclear dynamics can be treated independently on the $\mathscr{U}_{11}$, coupled $\mathscr{U}_{22}-\mathscr{U}_{33}$, and $\mathscr{U}_{44}$ electronic states. To reveal explicitly the impact of the nonadiabatic coupling on the nuclear dynamics in the $\mathscr{U}_{22}-\mathscr{U}_{33}$ electronic states, we perform companion calculations for the photoelectron transitions to the uncoupled $\mathscr{U}_{22}$ and $\mathscr{U}_{33}$ electronic states also and the results are compared to those obtained in the coupled-state simulations.

Because we start from an initial bound-state wave function, we calculate, $C(t) = \langle \chi^k(t/2)|\chi^k(t/2)\rangle$, which halves the total propagation time, T, needed to achieve the energy resolution, $\Delta E = 2\pi\hbar/T$, in the photoelectron spectrum.[39] To reproduce the broadening of the spectrum due to limited energy resolution in the experiment and also due to three-body rotation, we damp the autocorrelation function with an exponential function, $f(t) = \exp(-t/\tau)$, before Fourier transformation. This is equivalent to convoluting a stick energy spectrum with a Lorentzian function with full width at the half-maximum (fwhm) $\Gamma = 2\hbar/\tau$; τ being the relaxation time. In the following, this width is chosen to best match the observed broadening of the experimental band.

A. First Photoelectron Band. The potential energy surface of the $\tilde{X}^2B_1$ electronic state of F_2O^+ in the r_d-r_v plane is shown as a contour line diagram in Figure 1a. Superimposed on it is the anharmonic initial wave function of the ground vibrational level of the ground electronic state of F_2O. It can be seen that the FC transition promotes the latter very near to the equilibrium geometry of the final state.

The theoretical results on the first photoelectron band is shown in Figure 1c along with the experimental results in panel b. The WP is time evolved for a total of 1.1 ps. The variation of the absolute value of the time autocorrelation function is shown as an insert in panel c. The autocorrelation function revels strong quasiperiodic recurrences in time; the average spacing between the successive recurrences is ~32 fs, which results into a spacing of ~0.13 eV in the energy domain. The latter can be observed by inspecting the energy spectrum in Figure 1c. The average splitting between the dominant peaks is ~0.13 eV (~1048 cm^{-1}) to be compared to the experimental value of the symmetric stretch frequency (~1030 cm^{-1}) of F_2O^+ in the $\tilde{X}^2B_1$ electronic state.[12] This band does not reveal any progression along the bending mode at the resolution of the experiment. This fact is considered in the FC simulation of this band by Wang et al.,[12] and their anharmonic model yielded results in

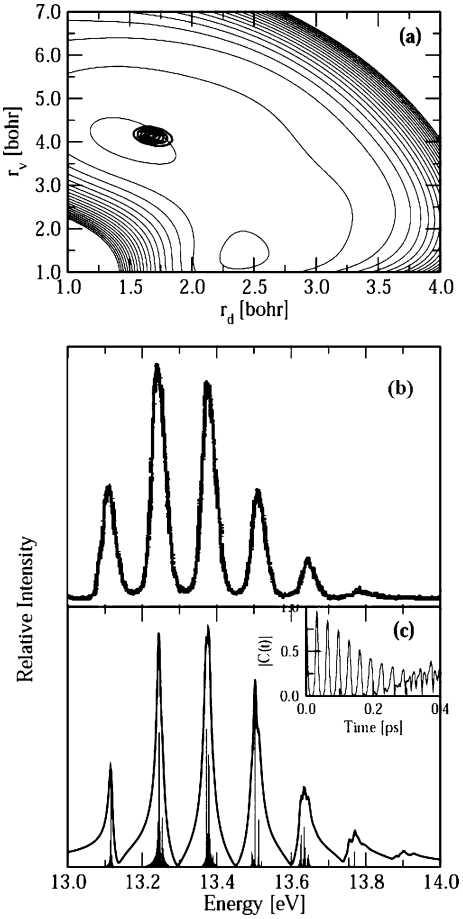

Figure 1. Contour line diagram of the potential energy surface of the $\tilde{X}^2B_1$ electronic state of F_2O^+ in the r_d-r_v plane (panel a). The potential energies are obtained from ref 12. The energy is measured relative to the minimum of the ground electronic state of F_2O. The minimum contour occurs at 0.5 eV and the spacing between the successive contour lines is 0.1 eV. The theoretical results on the first photoelectron band obtained by propagating the initial anharmonic wave function of the F_2O ground vibrational level of the ground electronic state (shown as dark solid contour lines in panel a) on the above electronic state is shown in panel c along with the available experimental results[12] in panel b. The variation of the absolute value of the time autocorrelation function is shown as an insert in panel c. Intensity in arbitrary units is plotted as a function of the ionization energy.

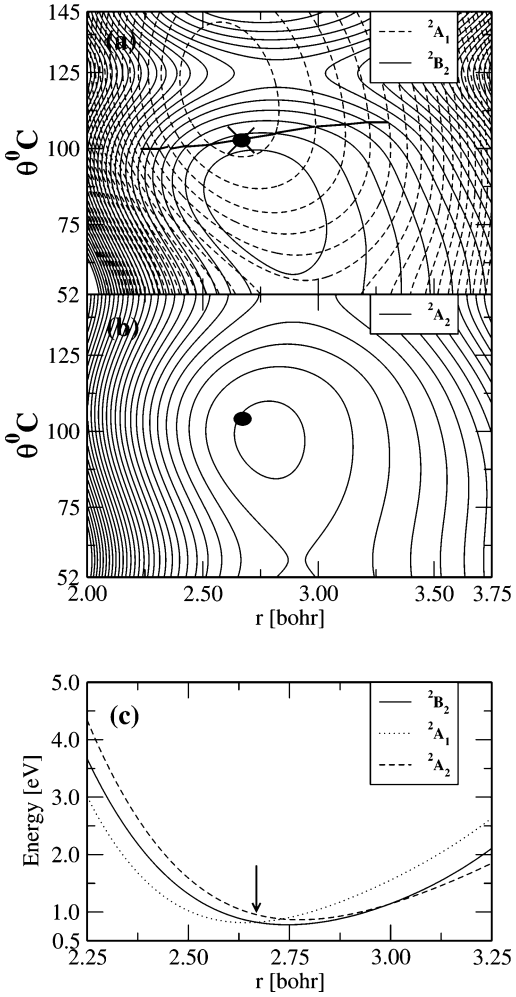

Figure 2. Contour line drawing of the $\tilde{A}^2B_2-\tilde{B}^2A_1$ and $\tilde{C}^2A_2$ (panel a and b, respectively) potential energy surfaces for C_{2v} geometries of F_2O^+. The spacing between the successive contour lines in 0.5 eV and the lowest energy contour occurs at 0.5 eV, 1.0 eV and ~0.83 eV for the $\tilde{A}^2B_2$, $\tilde{B}^2A_1$, and $\tilde{C}^2A_2$ ionic states, respectively. The zero of the energy scale corresponds to the minimum of the $\tilde{A}^2B_2$ state of F_2O^+. The seam of conical intersections between the $\tilde{A}^2B_2$ and $\tilde{B}^2A_1$ electronic states is shown by the solid line in panel a, and the cross on it indicates the energetic minimum of this seam. The heavy dots in panels a and b indicate the center of the FC zone in the photoionization to the respective state. One-dimensional cuts of the $\tilde{A}^2B_2$, $\tilde{B}^2A_1$, and $\tilde{C}^2A_2$ electronic states through the minimum of the intersection seam of panel a are plotted along the O−F bond distance and shown in panel c. The arrow in the panel points to the minimum of the seam of conical intersection between the $\tilde{A}^2B_2$ and $\tilde{B}^2A_1$ electronic states.

good accord with the experiment. The present time-dependent WP results are also in very good agreement at low energy resolution. The time autocorrelation function in Figure 1c is damped with a τ value of ~263 fs ($\Gamma = 5$ meV) to generate the spectral envelope. The Fourier transformation of the autocorrelation function without damping is also included in the figure. It can be seen that each peak in the broad envelope splits under high resolution, and we find even quantum progression along the bending vibrational mode corresponding to a frequency value of ~0.07 eV. The experimental value of the adiabatic ionization energy of the above band is ~13.11 eV; this is reproduced well in the theoretical results.

B. Overlapping Second, Third, and Fourth Photoelectron Bands and the Nonadiabatic Effects. The $\tilde{A}^2B_2$ electronic state of F_2O^+ is energetically lower than the $\tilde{B}^2A_1$ state at the equilibrium configuration. The latter is in turn energetically lower than the $\tilde{C}^2A_2$ state at the equilibrium geometry. The minimum of the $\tilde{A}^2B_2$ state is ~0.036 eV lower than that of the $\tilde{B}^2A_1$ state, which is ~0.05 eV lower than the $\tilde{C}^2A_2$ state. Therefore, it is clear that these states are very close in energy and the photoelectron bands arising from these three ionic states will be highly overlapping. In addition, the $\tilde{A}^2B_2$ and $\tilde{B}^2A_1$ ionic states can couple via the asymmetric stretching vibrational mode at sufficiently low energy.

The contour line diagram of the $\tilde{A}^2B_2$, $\tilde{B}^2A_1$, and $\tilde{C}^2A_2$ ionic states are shown in Figure 2a and b and plotted in the ($r-\theta$) plane to illustrate their topography for the C_{2v} geometrical arrangements of the nuclei. The potential energies are obtained from the ab initio potential energy function of Wang et al.[12] The energies are measured relative to the minimum of the $\tilde{A}^2B_2$ electronic state. The $\tilde{A}^2B_2$ and $\tilde{B}^2A_1$ electronic states can cross each other at the C_{2v} geometrical arrangements in the space of the totally symmetric vibrational modes and from conical intersections. The seam of conical intersections of these states is shown by the solid line in Figure 2a, and the cross on it indicates its energetic minimum occurring at ~0.83 eV. The center of the FC zone in this coupled electronic manifold is

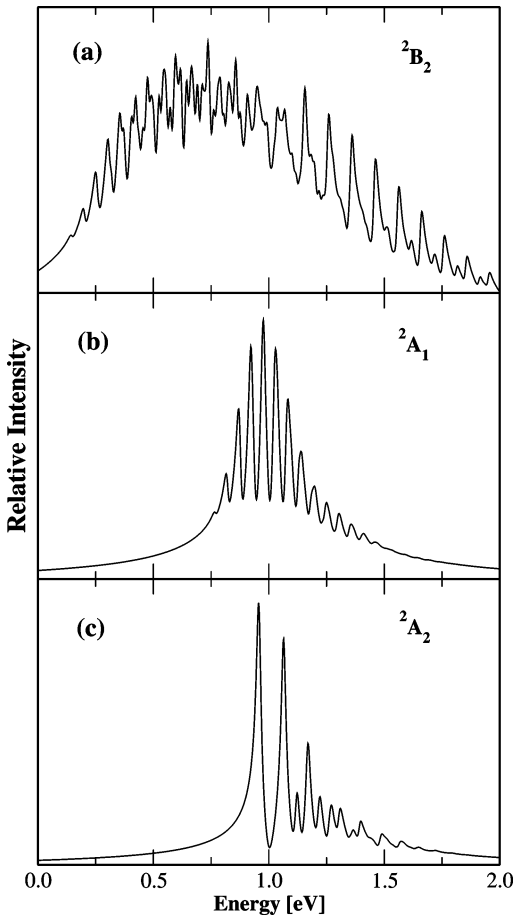

Figure 3. Photoelectron spectrum for the uncoupled (a) $\tilde{A}^2B_2$, (b) $\tilde{B}^2A_1$, and (c) $\tilde{C}^2A_2$ electronic states of F_2O^+. The spectral intensity (in arbitrary units) is plotted as a function of the energy of the final electronic state. The spectra are obtained with the anharmonic initial wave function (cf. Figure 1a) of F_2O. The zero of the energy scale corresponds to the minimum of the $\tilde{A}^2B_2$ electronic state.

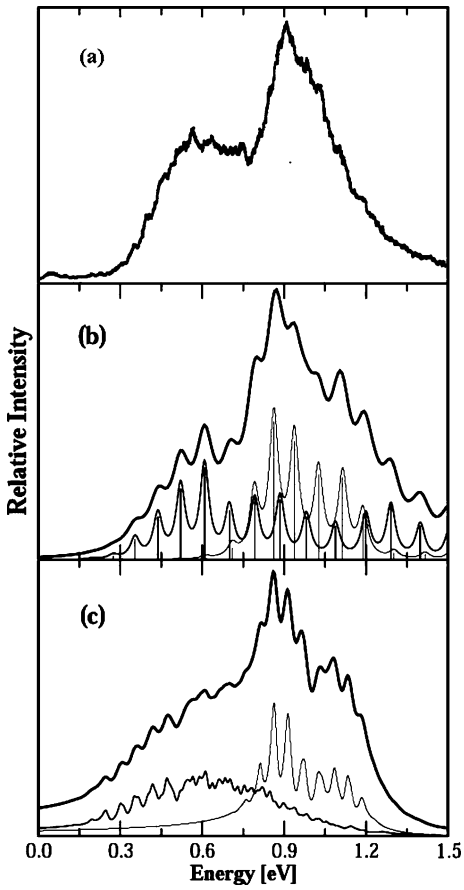

Figure 4. Composite photoelectron spectrum of F_2O corresponding to a transition to the three excited electronic states, $\tilde{A}^2B_2$, $\tilde{B}^2A_1$, and $\tilde{C}^2A_2$, of F_2O^+. The relative intensity in arbitrary units is plotted as a function of the energy of the final vibronic state. The experimental spectrum reproduced from ref 12 is shown in panel a. The composite theoretical photoelectron spectrum obtained by the Lanczos diagonalization method and using a harmonic initial wave function of the F_2O ground state is shown in panel b as dark solid lines. Similarly, in panel c, the composite theoretical band obtained by propagating the anharmonic initial wave function is shown. The two spectra due to the $\tilde{A}^2B_2$ (thick solid lines) and $\tilde{B}^2A_1$ (thin solid lines) electronic states obtained in the coupled-state situation are included in panels b and c under the theoretical composite band. The stick energy spectra obtained by the Lanczos diagonalization method are also included in panel b.

shown by the dot in Figure 2a and also in Figure 2b. It can be seen that the photoionization process prepares the WP almost on the intersection seam. Therefore, the latter is expected to be immediately perturbed by the associated nonadiabatic coupling effects. One-dimensional cuts of the above electronic states through the minimum of the seam of the intersections of Figure 2a are plotted along the O−F distance in Figure 2c. The minimum of the seam of intersections occurs at $r \approx 2.67\ a_0$ and $\theta \approx 102.69°$, and this minimum is relatively closer to the minimum of the $\tilde{B}^2A_1$ state occurring at $r \approx 2.62$ a_0 and $\theta \approx 119.5°$.[12] Therefore, the effect of the nonadiabatic coupling on the nuclear dynamics of the latter state is expected to be stronger. The near degeneracy of the $\tilde{C}^2A_2$ state and $\tilde{A}^2B_2-\tilde{B}^2A_1$ electronic states is also revealed in the figure.

In Figure 3a−c we show the photoelectron bands for the uncoupled $\tilde{A}^2B_2$, $\tilde{B}^2A_1$, and $\tilde{C}^2A_2$ electronic states of F_2O^+, respectively. The spectra are obtained by propagating the anharmonic initial wave function of the F_2O ground state on the above cationic states. The time autocorrelation function in each case is damped with $\tau \approx 8.5$ fs to generate the broad band envelopes in Figure 3a−c. We note that we also carried out the time-independent matrix diagonalization calculations in order to unambiguously identify the progressions in the above three spectra. In this case, however, a harmonic initial wave function is used. The theoretical data reveal an average spacing of ∼0.062 eV (∼500 cm^{-1}) between the intense lines in the $\tilde{A}^2B_2$ band. This can be attributed to the progression along the bending vibrational mode of F_2O^+. We also note that the time-dependent results in Figure 3a may also have finite background contributions arising from the direct dissociative component of the WP. A similar average energy spacing of ∼0.063 eV corresponding to a progression along the bending vibrational mode is also found in the $\tilde{B}^2A_1$ band (cf. Figure 3b). Similar extended progression along the bending vibrational mode is observed in the corresponding photoelectron bands of Cl_2O.[8] The dominant lines in the $\tilde{C}^2A_2$ band in Figure 3c, however, are ∼0.13 eV (∼1048 cm^{-1}) spaced in energy, which corresponds to the frequency of the symmetric stretching mode.

The final theoretical results (panel b and c) along with the experimental results (panel a)[12] are shown in Figure 4. First of all, the experimental band is highly diffuse and ionization to all three cationic electronic states contributes to the intensity of this band. Our theoretical results represent the full contribution from the $\tilde{A}^2B_2-\tilde{B}^2A_1$ electronic manifold and ∼10% contribution from the $\tilde{C}^2A_2$ electronic state to the overall spectral intensity. The composite photoelectron bands are shown by the thick solid lines in panels b and c. They are obtained by adding three spectra pertinent to the transitions to the above three

cationic states. The results in panel b are obtained by the Lanczos diagonalization method using a harmonic initial wave function of the F_2O ground electronic state constructed in terms of dimensionless normal coordinates. The results in panel c, however, are obtained by propagating the anharmonic initial WP on the final electronic states. The two spectra due to the $\tilde{A}^2B_2$ (thick solid lines) and $\tilde{B}^2A_1$ (thin solid lines) electronic states obtained in the coupled-state situation are included in each panel under the theoretical composite band. In addition, the stick energy spectra obtained by the Lanczos diagonalization method are included in panel b. The composite theoretical envelopes are obtained by introducing a broadening by convoluting with a Lorentzian function with $\Gamma = 40$ meV. It can be seen clearly that the $\tilde{A}^2B_2$ state contributes to the low-energy maximum and the $\tilde{B}^2A_1$ and $\tilde{C}^2A_2$ states contribute to the high-energy maximum of the observed bimodal intensity distribution in the experimental recording. The peaks in the coupled-state spectra of the $\tilde{A}^2B_2$ and $\tilde{B}^2A_1$ electronic states are somewhat broader than those obtained in the uncoupled-state situation (cf. Figure 3a and b, respectively). The band origin in the coupled-state situation shifts by ~0.05 eV and ~0.001 eV to the higher energy compared to those in the uncoupled-state situation for $\tilde{A}^2B_2$ and $\tilde{B}^2A_1$ electronic states, respectively. The broadening of the spectral peaks in the coupled-state situation (in comparison to the uncoupled-state results in Figure 3a and b) results from the nonadiabatic interactions between the two states.

The composite theoretical photoelectron bands in panels b and c contained ~10% contribution from the $\tilde{C}^2A_2$ state spectrum (cf. Figure 3c). We note that the heights of the two maxima in the theoretical band is adjusted empirically to fit with the experimental results. Such an adjustment was necessary as constant values of the transition dipole moment are assumed in the theoretical study. It is worth mentioning here that the nonadiabatic coupling strength in F_2O^+ is approximately two times larger than that found in Cl_2O^+.[8] This is the reason that the experimental photoelectron band of Cl_2O has more resolved structures than F_2O. The increased value of the nonadiabatic coupling definitely contributes to the broadening of the bands; however, the resolution in the experimental recording also has to be taken into account for the observed broadening.

The adiabatic ionization positions cannot be identified unambiguously in the experimental recording because of the highly overlapping nature of the composite band. Wang et al.[12] have predicted an adiabatic ionization energy of ~15.71 eV for this composite band. In our calculation, the first peak in the $\tilde{A}^2B_2$ spectrum observed at ~15.79 eV in the coupled-state situation, when energy is measured relative to the minimum of this state. The minimum of the $\tilde{A}^2B_2$ state of F_2O^+ is ~17.70 eV above that of the ground electronic state of F_2O.[12] Therefore, the present theoretical results overestimate the adiabatic ionization position of the band and can be further improved by refining the energy at the global minimum of these electronic states. To this end, we note that the agreement between the theoretical and experimental results are satisfactory within the mentioned approximations made in the theoretical treatment. The theoretical results may be further improved by carrying out full dimensional calculations of the potential energy surfaces, the electronic and relativistic spin−orbit coupling surfaces, and the relevant transition dipole moment surfaces. This is beyond the scope of the present investigations and may be considered in a future study.

To this end, we note that a referee suggested that we comment on the importance of the present full quantum dynamical treatment versus a similar approximate treatment within harmonic picture. Our observations reveal that the anharmonicity of the initial state does not alter the results significantly because we start from its ground vibrational and rotational level. However, the anharmonicity of the final electronic state (particularly in the coupled-state situation) is definitely more crucial for the observed asymmetry of the photoelectron band. Also, the broad and diffuse nature of the observed band implies a portion of the WP samples the dissociative region of the final electronic states (cf. Figure 6). The latter cannot be described properly by a harmonic model. Therefore, it is very important to consider realistic model of the final electronic states and perform a full quantum dynamical treatment of the nuclear dynamics.

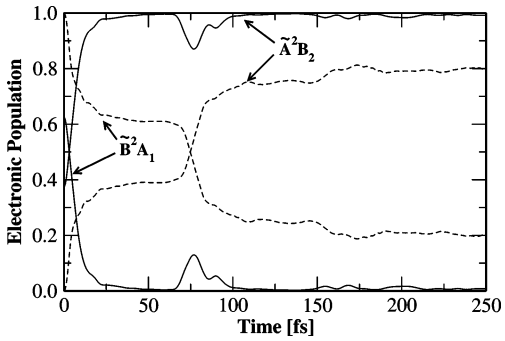

Figure 5. Time dependence of the adiabatic (solid lines) and diabatic (dashed lines) electronic populations in the coupled-state dynamics of the $\tilde{A}^2B_2-\tilde{B}^2A_1$ electronic states corresponding to an initial FC transition to the $\tilde{B}^2A_1$ electronic state of F_2O^+.

C. Time-Dependent Dynamics in the $\tilde{A}^2B_2-\tilde{B}^2A_1$ Electronic States of F_2O^+. To enunciate the impact of nonadiabatic coupling on the WP dynamics, we now report on the time dependence of the adiabatic and diabatic electronic populations in the $\tilde{A}^2B_2-\tilde{B}^2A_1$ coupled electronic states of F_2O^+. These populations are calculated by defining adiabatic projectors in the diabatic electronic representation.[15,36] The minimum of the $\tilde{B}^2A_1$ electronic state is closer to the seam of conical intersections (cf. Figure 2a), and therefore the dynamics of the initially prepared WP on this state is more strongly influenced by the nonadiabatic coupling compared to that on the $\tilde{A}^2B_2$ state. An initial location of the WP on the latter diabatic state corresponds to 63%: 37% population of the component adiabatic states at $t = 0$. In this case, only ~6% of the population moves to the $\tilde{B}^2A_1$ diabatic state and the population dynamics does not reveal any characteristic feature and, therefore, we do not show it here.

The population dynamics of the WP initially prepared on the $\tilde{B}^2A_1$ diabatic electronic state, however, reveals interesting features and is shown in Figure 5. The adiabatic and diabatic electronic populations are shown by the solid and dashed lines, respectively. Because the WP is initially located on the $\tilde{B}^2A_1$ diabatic electronic state, the population of this state is 1.0 at $t = 0$. This initial location also corresponds to 63%: 37% population of the component adiabatic states such as in the $\tilde{A}^2B_2$ case above. It can be seen that the $\tilde{B}^2A_1$ diabatic electronic population starting from 1.0 at $t = 0$ decays to ~0.2 at longer times. The initial decay of the population relates to a decay time of ~30 fs for this state. The population decays to ~0.63 at ~25 fs; therefore, within this time about 37% of the population moves to the $\tilde{A}^2B_2$ diabatic state; population of this state starts from zero at $t = 0$. The population of both of these states does not vary noticeably afterward until ~70 fs, when a second sharp drop in the $\tilde{B}^2A_1$ diabatic population takes place. Within about ~100 fs, ~73% of the population reaches to the $\tilde{A}^2B_2$ diabatic state. The population of the two component

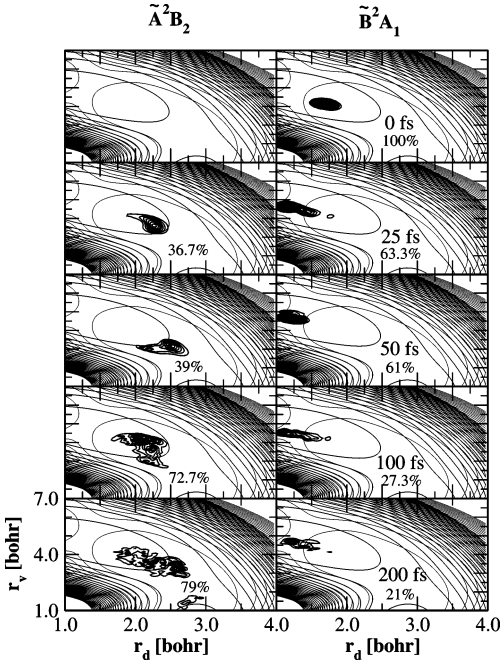

Figure 6. Probability density ($|\chi^k|^2$) of the diabatic WP averaged over the angular coordinate and superimposed on the potential energy contours in the (r_d-r_v) plane for $\gamma = \pi/2$ in the coupled-state dynamics of Figure 5. The WP components on the $\tilde{A}^2B_2$ and $\tilde{B}^2A_1$ electronic states at a given time (indicated in each panel) are shown in the left and right panels, respectively.

adiabatic states reaches ~100%: 0.0% at longer times. The weak recurrences seen in the adiabatic electronic populations are damped in the diabatic ones.

To better understand the above population dynamics, we show snapshots of the wave packet evolving on the coupled $\tilde{A}^2B_2-\tilde{B}^2A_1$ diabatic electronic states at different times in Figure 6. The contours of the probability density ($|\chi^k|^2$) of the WP averaged over the angular coordinate is superimposed on the potential energy contours for $\gamma = \pi/2$ in the r_d-r_v plane. It can be seen that the WP at $t = 0$ is located very near to the equilibrium geometry of the $\tilde{B}^2A_1$ electronic state. The latter is found to be closer to the seam of $\tilde{A}^2B_2-\tilde{B}^2A_1$ conical intersections (cf. Figure 2a). Because of this, the internal conversion to the $\tilde{A}^2B_2$ state takes place within a very short time. It can be seen that ~37% of the WP moves to this state within ~25 fs. The portion of the WP in the $\tilde{A}^2B_2$ state approaches toward the energetic minimum of this state (cf. snapshots at ~50 fs) after arrival and mostly remain there at longer times. It appears that once the WP reaches the $\tilde{A}^2B_2$ state most of it does not recross the intersection seam and move to the $\tilde{B}^2A_1$ electronic state again. This is also indicated by the absence of quasiperiodic recurrences in the time dependence of the electronic populations (cf. Figure 5). At longer time (~200 fs), ~79% of the WP moves to the $\tilde{A}^2B_2$ electronic state.

V. Summary and Outlook

We have presented a theoretical account on the photoelectron spectroscopy of F_2O and compared our findings to the available experimental results. Particularly, the effects due to possible nonadiabatic interactions between the $\tilde{A}^2B_2$ and $\tilde{B}^2A_1$ electronic states of F_2O^+ on the photoelectron bands are examined in detail. The theoretical approach is based on the relevant ab initio potential energy surfaces of the system and time-independent and time-dependent quantum dynamical methods.

In this study, the near equilibrium C_{2v} PESs reported by Wang et al.[12] for the F_2O ground and the low-lying excited electronic states of F_2O^+ are extended to the C_s geometries, assuming a harmonic contribution from the asymmetric stretching vibrational mode. This is motivated by the fact that the excitation along this vibrational mode is not observed in the experimental data.[12]

Analysis of the first photoelectron band revealed dominant progression along the symmetric stretch vibration. Weak excitations of the even quantum of bending vibration are also observed under high energy resolution. The broad-band spectral envelope compares well with the experimental results. The second, third, and fourth photoelectron bands are highly overlapping and are due to ionizations to the near-degenerate $\tilde{A}^2B_2$, $\tilde{B}^2A_1$, and $\tilde{C}^2A_2$ electronic states of F_2O^+, respectively. The nonadiabatic interactions between the $\tilde{A}^2B_2$ and $\tilde{B}^2A_1$ ionic states are modeled here within a linear coupling scheme. These two ionic states can be coupled via the asymmetric stretching vibration. Conical intersections between these two states are established. The strength of the coupling parameter is derived from the electronic structure results. This resulted in the estimate 0.05 eV $\leq \lambda \leq$ 0.28 eV, with 0.18 eV as an average value of this quantity. The photoelectron bands due to $\tilde{A}^2B_2$ and $\tilde{B}^2A_1$ ionic states reveal extended progression along the bending vibrational mode. The nonadiabatic interactions between these states contribute largely to the observed diffuse structure of the experimental band. The photoelectron band due to the $\tilde{C}^2A_2$ ionic state reveals dominant progression along the symmetric stretching vibration. The relativistic spin−orbit interactions of this state with the $\tilde{B}^2A_1$ ionic state is not considered in this study. We assumed ~10% contribution due to this state in the overall composite theoretical results presented here. The theoretical results are in good accord with the observed experimental results. Experimental results at higher energy resolutions are desirable to further refine the present theoretical model.

Acknowledgment. This study was supported in part by a research grant from the Council of Scientific and Industrial Research (Grant no. 01(1917)/04/EMR-11), New Delhi. Thanks are due to K. Jagadishwara Reddy for his assistance. S.G. acknowledges the University Grants Commission (UGC), New Delhi, for a Senior Research Fellowship. We also thank UGC (the UPE program) and Department of Science and Technology (the High Performance Computational Facilities Program) for the computational facilities provided in the University of Hyderabad.

References and Notes

(1) (a) Molina, M. J.; Rowland, F. S. *Nature* (*London*) **1974**, *249*, 810. (b) Vaida, V.; Solomon, S.; Richard, E. C.; Ruhl, E.; Jefferson, A. *Nature* (*London*) **1989**, *342*, 405. (c) Rowland, F. S. *Annu. Rev. Phys. Chem.* **1991**, *42*, 731 and references therein.

(2) (a) Vaida, V.; Simon, J. D. *Science* **1995**, *268* 1443. (b) Davis, H. F.; Lee, Y. T. *J. Phys. Chem.* **1992**, *96*, 5681. (c) *J. Chem. Phys.* **1996**, *105*, 8142. (d) Reid, P. J. *Acc. Chem. Res.* **2001**, *34*, 691. (e) Gilles, M. K.; Polak, M. L.; Lineberger, W. C. *J. Chem. Phys.* **1996**, *96*, 8102. (f) Wang, X.-B.; Wang, L.-S. *J. Chem. Phys.* **2001**, *113*, 10928.

(3) Motte-Tollet, F.; Delwiche, J.; Heinesch, J.; Hubin-Franskin, M.-J.; Gingell, J. M.; Jones, N. C.; Mason, N. J.; Marston, G. *Chem. Phys. Lett.* **1998**, *284*, 452.

(4) (a) Peterson, K. A.; Werner, H.-J. *J. Chem. Phys.* **1992**, *96*, 8948. (b) Peterson, K. A.; Werner, H.-J. *J. Chem. Phys.* **1993**, *99*, 302. (c) Peterson, K. A.; Werner, H.-J. *J. Chem. Phys.* **1996**, *105*, 9823. (d) Peterson, K. A. *J. Chem. Phys.* **1998**, *109*, 8864.

(5) (a) Wang, D.-C.; Lee, E. P. F.; Chau, F.-T.; Mok, D. K. W.; Dyke, J. M. *J. Phys. Chem. A* **2000**, *104*, 4936. (b) Mok, D. K. W.; Lee, E. P. F.; Chau, F.-T.; Wang, D.-C.; Dyke, J. M. *J. Chem. Phys.* **2000**, *113*, 5791.

(6) Mahapatra, S.; Krishnan, G. M. *J. Chem. Phys.* **2001**, *115*, 6951.

(7) (a) Krishnan, G. M.; Mahapatra, S. *J. Chem. Phys.* **2003**, *118*, 8715. (b) Mahapatra, S.; Ritschel, Th. *Chem. Phys.* **2003**, *289*, 291.
(8) Mahapatra, S. *J. Chem. Phys.* **2002**, *116*, 8817.
(9) Mahapatra, S. *Int. Rev. Phys. Chem.* **2004**, *23*, 483.
(10) Conford, A. B.; Frost, D. C.; Herring, F. G.; McDowell, C. A. *J. Chem. Phys.* **1971**, *55*, 2820.
(11) Brundle, C. R.; Robin, M. B.; Kuebler, N. A.; Basch, H. *J. Am. Chem. Soc.* **1972**, *94*, 1451.
(12) Wang, D.-C.; Chau, F.-T.; Mok, D. K.-W.; Lee, E. P. F.; Beeching, L.; Ogden, J. S.; Dyke, J. M. *J. Chem. Phys.* **2001**, *114*, 10682.
(13) (a) von Niessen, W. *J. Electron Spectrosc. Relat. Phenom.* **1979**, *17*, 197. (b) Valenta, K. E.; Vasudevan, K.; Grein, F. *J. Chem. Phys.* **1980**, *72*, 2148. (c) Langhoff, S. R.; Chong, D. P. *Chem. Phys. Lett.* **1982**, *86*, 487. (d) Decleva, P.; Lisini, A. *Chem. Phys.* **1986**, *106*, 39. (e) Hu, C.-H.; Chong, D. P.; Casida, M. E. *J. Electron Spectrosc. Relat. Phenom.* **1997**, *85*, 39.
(14) (a) Tomasello, P.; Ehara, M.; Nakatsuji, H. *J. Chem. Phys.* **2002**, *116*, 2425. (b) Tomasello, P.; Ehara, M.; Nakatsuji, H. *J. Chem. Phys.* **2003**, *118*, 5811.
(15) Köppel, H.; Domcke, W.; Cederbaum, L. S. *Adv. Chem. Phys.* **1984**, *57*, 59.
(16) (a) Kosloff, R. *J. Phys. Chem.* **1988**, *92*, 2087. (b) Balakrishnan, N.; Kalyanaraman, C.; Satyamurthy, N. *Phys. Rep.* **1997**, *280*, 79 and references therein. (c) Mahapatra, S.; Chakrabarti, N.; Sathyamurthy, N. *Int. Rev. Phys. Chem.* **1999**, *18*, 235.
(17) Cullum, J.; Willoughby, R. *Lanczos Algorithms for Large Symmetric Eigenvalue Problems*; Birkhäuser: Boston, MA, 1985; Vols. I and II.
(18) Mahapatra, S. Vibronic Coupling and Nonadiabatic Molecular Dynamics. In *Reviews in Modern Quantum Chemistry: A Celebration of the Contributions of Robert Parr*; Sen, K. D., Ed.; World Scientific: Singapore, 2002; pp 359−400.
(19) *Conical Intersections: Electronic Structure, Dynamics and Spectroscopy*; Domcke, W., Yarkony, D. R., Köppel, H., Eds.; World Scientific: Singapore, 2004.
(20) (a) Lichten, W. *Phys. Rev.* **1967**, *164*, 131. (b) Smith, F. T. *Phys. Rev.* **1969**, *179*, 111. (c) O'Malley, T. F. *Adv. Atomic Mol. Phys.* **1971**, *7*, 223. (d) Pacher, T.; Cederbaum L. S.; Köppel, H. *Adv. Chem. Phys.* **1993**, *84*, 293 and references therein.
(21) Pack, R. T.; Parker, G. A. *J. Chem. Phys.* **1987**, *87*, 3888.
(22) Wilson, E. B., Jr.; Decius, J. C.; Cross, P. C. *Molecular Vibrations*; McGraw-Hill: New York, 1955.
(23) Pierce, L.; DiCianni, N.; Jackson, R. *J. Chem. Phys.* **1963**, *38*, 730.
(24) Dunning, T. H., Jr. *J. Chem. Phys.* **1989**, *90*, 1007.
(25) Frisch, M. J.; Trucks, G. W.; Schlegel, H. B.; Scuseria, G. E.; Robb, M. A.; Cheeseman, J. R.; Montgomery, J. A., Jr.; Vreven, T.; Kudin, K. N.; Burant, J. C.; Millam, J. M.; Iyengar, S. S.; Tomasi, J.; Barone, V.; Mennucci, B.; Cossi, M.; Scalmani, G.; Rega, N.; Petersson, G. A.; Nakatsuji, H.; Hada, M.; Ehara, M.; Toyota, K.; Fukuda, R.; Hasegawa, J.; Ishida, M.; Nakajima, T.; Honda, Y.; Kitao, O.; Nakai, H.; Klene, M.; Li, X.; Knox, J. E.; Hratchian, H. P.; Cross, J. B.; Bakken, V.; Adamo, C.; Jaramillo, J.; Gomperts, R.; Stratmann, R. E.; Yazyev, O.; Austin, A. J.; Cammi, R.; Pomelli, C.; Ochterski, J. W.; Ayala, P. Y.; Morokuma, K.; Voth, G. A.; Salvador, P.; Dannenberg, J. J.; Zakrzewski, V. G.; Dapprich, S.; Daniels, A. D.; Strain, M. C.; Farkas, O.; Malick, D. K.; Rabuck, A. D.; Raghavachari, K.; Foresman, J. B.; Ortiz, J. V.; Cui, Q.; Baboul, A. G.; Clifford, S.; Cioslowski, J.; Stefanov, B. B.; Liu, G.; Liashenko, A.; Piskorz, P.; Komaromi, I.; Martin, R. L.; Fox, D. J.; Keith, T.; Al-Laham, M. A.; Peng, C. Y.; Nanayakkara, A.; Challacombe, M.; Gill, P. M. W.; Johnson, B.; Chen, W.; Wong, M. W.; Gonzalez, C.; Pople, J. A. *Gaussian 03*, revision B.05; Gaussian, Inc.: Wallingford, CT, 2004.
(26) Domcke, W.; Köppel, H.; Cederbaum, L. S. *Mol. Phys.* **1981**, *43*, 851.
(27) Heller, E. J. *Acc. Chem. Res.* **1981**, *14*, 368.
(28) Feit, M. D.; Fleck, J. A., Jr.; Steiger A. *J. Comput. Phys.* **1982**, *47*, 412.
(29) (a) Varandas, A. J. C.; Yu, H.-G. *Chem. Phys. Lett.* **1996**, *259*, 336. (b) Mahapatra, S.; Köppel, H. *J. Chem. Phys.* **1998**, *109*, 1721. (c) Ghosal, S.; Mahapatra, S. *J. Chem. Phys.* **2004**, *121*, 5740.
(30) Kosloff, D.; Kosloff, R. *J. Comput. Phys.* **1983**, *52*, 35.
(31) Bačić, Z.; Light, J. C. *Annu. Rev. Phys. Chem.* **1989**, *40*, 469.
(32) Mahapatra, S.; Sathyamurthy, N. *J. Chem. Soc., Faraday Trans.* **1997**, *93*, 773.
(33) Kosloff, R.; Tal-Ezer, H. *Chem. Phys. Lett.* **1986**, *127*, 223.
(34) Park, T. J.; Light, J. C. *J. Chem. Phys.* **1986**, *85*, 5870.
(35) Domcke, W.; Stock, G. *Adv. Chem. Phys.* **1997**, *100*, 1.
(36) (a) Manthe, U.; Köppel, H. *J. Chem. Phys.* **1990**, *93*, 345. (b) Manthe, U.; Köppel, H. *J. Chem. Phys.* **1990**, *93*, 1685.
(37) Köppel, H.; Domcke, W. *Encyclopedia of Computational Chemistry*; Schleyer, P. v. R., Ed.; Wiley: New York, 1998.
(38) (a) Wall, M. R.; Neuhauser, D. *J. Chem. Phys.* **1995**, *102*, 8011. (b) Mandelshtum, V. A.; Taylor, H. S. *Phys. Rev. Lett.* **1997**, *78*, 3274. (c) Mandelshtum, V. A.; Taylor, H. S. *J. Chem. Phys.* **1997**, *107*, 6756.
(39) (a) Manthe, U.; Meyer, H.-D.; Cederbaum, L. S. *J. Chem. Phys.* **1992**, *97*, 3199. (b) Engel, V. *Chem. Phys. Lett.* **1992**, *189*, 76.